Monthly Notices of the ROYAL ASTRONOMICAL SOCIETY

MNRAS **530,** 2512–2525 (2024) https://doi.org/10.1093/mnras/stae969
Advance Access publication 2024 April 10

Extending the chemical reach of the H3 survey: detailed abundances of the dwarf-galaxy stellar stream Wukong/LMS-1†

Guilherme Limberg [1,2,3]★ Alexander P. Ji [2,3] Rohan P. Naidu,[4] Anirudh Chiti,[2,3] Silvia Rossi [1] Sam A. Usman,[2,3] Yuan-Sen Ting(丁源森) [5,6,7] Dennis Zaritsky [8] Ana Bonaca [9] Lais Borbolato,[1] Joshua S. Speagle(沈佳士),[10,11,12,13] Vedant Chandra [14] and Charlie Conroy[14]

[1]*IAG, Departamento de Astronomia, Universidade de São Paulo, SP 05508-090 São Paulo, Brazil*
[2]*Department of Astronomy and Astrophysics, University of Chicago, 5640 S Ellis Avenue, Chicago, IL 60637, USA*
[3]*Kavli Institute for Cosmological Physics, University of Chicago, Chicago, IL 60637, USA*
[4]*Department of Physics and Kavli Institute for Astrophysics and Space Research, Massachusetts Institute of Technology, Cambridge, MA 02139, USA*
[5]*Research School of Astronomy and Astrophysics, Australian National University, Weston, ACT 2611 Canberra, Australia*
[6]*School of Computing, Australian National University, Acton, ACT 2601 Canberra, Australia*
[7]*Department of Astronomy, The Ohio State University, 140 West 18th Avenue, Columbus, OH 43210, USA*
[8]*Steward Observatory, University of Arizona, 933 N. Cherry Ave., Tucson, AZ 85721-0065, USA*
[9]*Observatories of the Carnegie Institution for Science, 813 Santa Barbara Street, Pasadena, CA 91101, USA*
[10]*Department of Statistical Sciences, University of Toronto, Toronto, ON M5G 1Z5, Canada*
[11]*David A. Dunlap Department of Astronomy and Astrophysics, University of Toronto, Toronto, ON M5S 3H4, Canada*
[12]*Dunlap Institute for Astronomy and Astrophysics, University of Toronto, Toronto, ON M5S 3H4, Canada*
[13]*Data Sciences Institute, University of Toronto, Toronto, ON M5G 1Z5, Canada*
[14]*Center for Astrophysics, Harvard and Smithsonian, 60 Garden Street, Cambridge, MA 02138, USA*

Accepted 2024 April 5. Received 2024 April 2; in original form 2023 August 30

ABSTRACT

We present the first detailed chemical-abundance analysis of stars from the dwarf-galaxy stellar stream Wukong/LMS-1 covering a wide metallicity range ($-3.5 < \mathrm{[Fe/H]} \lesssim -1.3$). We find abundance patterns that are effectively indistinguishable from the bulk of Indus and Jhelum, a pair of smaller stellar streams proposed to be dynamically associated with Wukong/LMS-1. We confirmed a carbon-enhanced metal-poor star ($\mathrm{[C/Fe]} > +0.7$ and $\mathrm{[Fe/H]} \sim -2.9$) in Wukong/LMS-1 with strong enhancements in Sr, Y, and Zr, which is peculiar given its solar-level [Ba/Fe]. Wukong/LMS-1 stars have high abundances of α elements up to $\mathrm{[Fe/H]} \gtrsim -2$, which is expected for relatively massive dwarfs. Towards the high-metallicity end, Wukong/LMS-1 becomes α-poor, revealing that it probably experienced fairly standard chemical evolution. We identified a pair of N- and Na-rich stars in Wukong/LMS-1, reminiscent of multiple stellar populations in globular clusters. This indicates that this dwarf galaxy contained at least one globular cluster that was completely disrupted in addition to two intact ones previously known to be associated with Wukong/LMS-1, which is possibly connected to similar evidence found in Indus. From these $\geq$3 globular clusters, we estimate the total mass of Wukong/LMS-1 to be $\approx 10^{10}$ $M_\odot$, representing $\sim$1 per cent of the present-day Milky Way. Finally, the [Eu/Mg] ratio in Wukong/LMS-1 continuously increases with metallicity, making this the first example of a dwarf galaxy where the production of *r*-process elements is clearly dominated by delayed sources, presumably neutron-star mergers.

Key words: stars: abundances – Galaxy: halo – Galaxy: kinematics and dynamics – galaxies: dwarf – Local Group.

1 INTRODUCTION

In a cold dark matter-dominated cosmology, massive Milky Way-like haloes are built up through successive accretion of dwarf galaxies (Searle & Zinn 1978; Faber & Gallagher 1979; White & Frenk 1991; Kauffmann, White & Guiderdoni 1993; Johnston 1998; Springel, Frenk & White 2006). Therefore, a fundamental prediction of this hierarchical paradigm is that satellite galaxies around any massive host present themselves as intact dwarfs, phase-mixed substructures, or in an intermediary stage as stellar streams (Bullock & Johnston 2005; Cooper et al. 2010, 2013; Pillepich, Madau & Mayer 2015; Morinaga et al. 2019).

Because the evolution of these dwarf galaxy streams and substructures was interrupted due to the shutdown of their star formation at the moment of their accretion, they provide a unique local window into the properties of galaxies that existed at high redshift (Boylan-Kolchin et al. 2015, 2016). Also, as these systems sample a wide range of stellar masses ($10^6 \lesssim M_\star/M_\odot < 10^9$; see Naidu et al. 2022; Sharpe, Naidu & Conroy 2022), they provide a laboratory for us to test the universality of galaxy formation/evolution processes as we can compare them with observations of intact dwarfs in

★ E-mail: guilherme.limberg@usp.br
† This paper includes data gathered with the 6.5 meter Magellan Telescopes located at Las Campanas Observatory, Chile.

the Local Group (Tolstoy, Hill & Tosi 2009; Simon 2019 for reviews). Conveniently, this approach comes with the advantage that member stars of these disrupted dwarfs are typically much closer and, hence, brighter than their counterparts located in surviving Milky Way satellites. This makes them more easily accessible to high-resolution ($\mathcal{R} \geq 20{,}000$) spectroscopy, from which detailed chemical abundances can be obtained for significant amounts of stars, allowing us to understand the properties of their progenitor systems. This 'near-field' approach to galaxy evolution at the smallest scales is even more appealing given that not even current and future facilities (such as *JWST* or 20–30 m ground telescopes) will be able to spatially resolve such low-mass galaxies at the redshift range ($0.5 < z \leq 2.0$) probed by these halo debris (Myeong et al. 2018, 2019; Koppelman et al. 2019a; Forbes 2020; Kruijssen et al. 2020; Naidu et al. 2020; Callingham et al. 2022, see also Naidu et al. 2021 for a relevant discussion).

The advent of astrometric information for more than a billion stars due to the *Gaia* space mission (Gaia Collaboration 2016a, b, 2018, 2021, 2022), in particular its second and third data releases (DR2 and DR3, respectively), in combination with large-scale photometric and spectroscopic surveys, has allowed the discovery of a myriad of accreted substructures in the Galactic halo (see Koppelman et al. 2019b, Malhan et al. 2022 and the stellar-stream compilation by Mateu 2023). Out of these, the most well-characterized disrupted dwarfs with detailed chemistry are, by far, *Gaia*-Sausage/Enceladus (GSE; Belokurov et al. 2018; Haywood et al. 2018; Helmi et al. 2018) and Sagittarius stream (e.g. Majewski et al. 2003), the tidal tails of Sagittarius dwarf spheroidal (dSph) galaxy (Ibata, Gilmore & Irwin 1994). Examples of such efforts include, but are not limited to, Monty et al. (2020), Aguado et al. (2021b), Matsuno et al. (2021), and Buder et al. (2022) for GSE, Hasselquist et al. (2019) and Hayes et al. (2020) for Sagittarius, and Hasselquist et al. (2021) and Horta et al. (2023) for both. Apart from these major substructures, other disrupted dwarfs with available high-resolution spectroscopy include Helmi streams (Helmi et al. 1999; see Roederer et al. 2010, Aguado et al. 2021a, Limberg et al. 2021, and Matsuno et al. 2022b for abundances), Orphan stream (Belokurov et al. 2006, 2007; e.g. Casey et al. 2014; Hawkins et al. 2023), and Sequoia[1] (Matsuno, Aoki & Suda 2019; Myeong et al. 2019; Matsuno et al. 2022a). For smaller stellar streams, the largest homogeneous study was presented by Ji et al. (2020a).

In this contribution, we present the first detailed chemical abundance analysis of Wukong/LMS-1 (Naidu et al. 2020; Yuan et al. 2020; Malhan et al. 2021). This substructure was identified by Yuan et al. (2020) who named it the 'low-mass stellar-debris stream 1' (LMS-1). Independently, Naidu et al. (2020) identified 'Wukong',[2] a prominent group of stars in integrals-of-motion space apparently dissociated from any previously known disrupted dwarf. The connection between LMS-1 and Wukong was quickly recognized for their indistinguishable dynamics, including the association with at least two globular clusters, NGC 5024 (M53) and NGC 5053, and two other stellar streams, Indus and Jhelum (Shipp et al. 2018; Bonaca et al. 2019, 2021; Malhan et al. 2022). Out of the known disrupted dwarf galaxies, some listed above, Wukong/LMS-1 is especially interesting due to its predicted relatively high stellar mass of $\sim 10^7\ M_\odot$ (Malhan et al. 2021), which is similar to classical Milky Way satellites such as Sculptor and Fornax dSph galaxies (McConnachie 2012). Therefore, our goal is to constrain Wukong/LMS-1's star-formation history, its production of the heaviest elements via prompt and/or delayed sources of neutron-capture processes, and even look for signatures of dissolved globular clusters in it. Then, we put our results in context by comparing with known Milky Way satellite galaxies of similar mass as well as chemical-evolution models.

This work is organized as follows. Section 2 includes all things related to our observations, data reduction, and radial velocity (RV) measurements. Our methodology for obtaining stellar parameters and abundances from high-resolution spectra is described in Section 3. Section 4 is reserved for the presentation of our results. In Section 5, we provide our concluding remarks and a brief discussion.

2 DATA

2.1 Observations

We observed 13 Wukong/LMS-1 targets (Wuk_1 to _13),[3] which were selected as best-suited for covering a wide metallicity range within the telescope time allocation available. These were originally identified by Naidu et al. (2020) using data from the Hectochelle in the Halo at High Resolution (H3) survey (Conroy et al. 2019), including orbital energy and angular momentum criteria, but also an [Fe/H] < -1.45 cut to avoid contamination by GSE stars. The observed sample is also contained in the 'high signal-to-noise' (high-*S*/*N*) sample of Wukong/LMS-1 stars from Johnson et al. (2022), also with H3 data, who refined Naidu et al.'s (2020) selection. All stars are also bright enough ($15 <$ *Gaia*'s $G \lesssim 16$) for high-resolution spectroscopy with our setup (see below). We collected spectra for an extra metal-rich ([Fe/H] ~ -1.3) Wukong/LMS-1 star (Wuk_14; Table 1) at $G \approx 15$ found in the Apache Point Observatory Galactic Evolution Experiment (APOGEE; Majewski et al. 2017) DR17 catalogue (Abdurro'uf et al. 2022). In order to guarantee that this additional target is a genuine Wukong/LMS-1 member, not a GSE interloper, we searched APOGEE for stars that respected the combined criteria from Naidu et al. (2020) and Johnson et al. (2022) as well as Yuan et al. (2020), which was developed independently from the H3 survey papers. The full criteria is written below. Because GSE-like mergers are not expected to deposit debris on such acute polar orbits (see Amarante et al. 2022, Limberg et al. 2023 for discussion), we can be confident that our APOGEE metal-rich target is a genuine member of Wukong/LMS-1.

In Fig. 1, we exhibit all our targets in projected action space within the McMillan (2017) Galactic model potential. The action vector is written as $\boldsymbol{J} = (J_R, J_\phi, J_z)$, where J_R, J_ϕ, and J_z are the radial, azimuthal, and vertical components in a cylindrical frame. Both of the abovementioned Wukong/LMS-1 samples and the globular clusters NGC 5024 and NGC 5053 are also plotted. For these orbit calculations, we integrated for 20 Gyr forward using the `AGAMA` library (Vasiliev 2019). Positions and proper motions on the sky are from *Gaia* DR3. RVs were determined by us for the stars we observed (see below). Other RVs employed were taken from their parent samples. Distances come from spectrophotometric fits, `MINESWEEPER` (Cargile et al. 2020) for H3 and `STARHORSE` (Queiroz et al. 2020, 2023) for APOGEE. For NGC 5024 and NGC

[1]Although we list Sequoia as an independent disrupted dwarf, we recognize the current dispute in the literature regarding whether or not this population could simply be part of the more massive GSE (Koppelman, Bos & Helmi 2020; Amarante et al. 2022; Limberg et al. 2022; Horta et al. 2023).

[2]Named after Sun Wukong, the celestial Monkey King from *Journey to the West*. See Naidu et al. (2020) for the complete rationale.

[3]Throughout this work, we use the 'Wuk' prefix followed by a natural number as unique names for stars in our sample (see Table 1).

Table 1. Observational information, RVs, and stellar parameters for Wukong/LMS-1 stars analysed in this work. The reported *S/N* values are per pixel. Model atmosphere metallicity values ([M/H]) can be larger than [Fe/H] by up to 0.03 dex.

Star	*Gaia* DR3 source_id	R.A. (deg)	Decl. (deg)	RV_{MIKE} ($km\,s^{-1}$)	*S/N* (4500Å)	*S/N* (6500Å)	T_{eff} (K)	$\sigma_{T_{eff}}$ (K)	log *g* (cgs)	$\sigma_{\log g}$ (cgs)	v_t ($km\,s^{-1}$)	σ_{v_t} ($km\,s^{-1}$)	[M/H]	$\sigma_{[M/H]}$
Wuk_1	2 721 020 906 259 820 416	332.6634	6.6813	−245.22	44	85	4887	103	2.12	0.50	1.58	0.11	−1.75	0.24
Wuk_2	2 671 790 891 601 429 376	322.1504	−5.4919	−96.59	30	68	4623	102	1.48	0.50	2.14	0.12	−1.91	0.25
Wuk_3	2 616 761 777 740 644 864	329.9007	−10.9341	−173.24	31	60	4866	104	1.90	0.51	1.62	0.12	−2.32	0.26
Wuk_4	4 424 978 984 005 490 304	240.3206	3.6775	87.79	30	60	5101	118	2.30	0.53	1.79	0.11	−2.89	0.24
Wuk_5	6 337 489 231 846 231 296	222.7506	−4.8440	2.70	37	72	4670	102	1.50	0.50	1.59	0.11	−2.41	0.25
Wuk_6	4 415 232 603 696 493 696	230.8720	−2.0148	−180.10	30	59	5307	148	3.15	0.57	1.51	0.16	−3.57	0.22
Wuk_7	3 614 246 079 443 061 376	210.9729	−11.2984	−56.56	21	46	5095	159	2.43	0.59	0.93	0.10	−2.93	0.28
Wuk_8	3 635 197 617 107 624 448	201.3197	−4.8245	233.76	34	56	5312	111	2.75	0.51	1.43	0.12	−1.98	0.26
Wuk_9	3 625 337 025 031 068 544	199.5284	−7.8565	98.30	30	53	4974	106	2.22	0.51	1.80	0.11	−2.01	0.26
Wuk_10	3 810 150 429 850 681 984	168.4136	0.8518	193.73	39	64	4814	101	1.90	0.50	1.55	0.11	−1.98	0.23
Wuk_11	1 225 051 430 189 620 864	213.3937	10.0073	4.00	39	71	4706	102	1.18	0.50	1.96	0.11	−2.37	0.23
Wuk_12	3 727 823 702 151 504 896	209.6407	12.8460	25.68	33	58	4842	103	1.82	0.50	1.77	0.11	−2.09	0.25
Wuk_13	3 737 533 184 394 415 232	197.0257	12.7782	93.73	34	61	4923	103	2.15	0.50	1.70	0.11	−1.87	0.27
Wuk_14	3 696 527 104 395 430 016	187.9680	0.0382	49.87	43	68	5099	100	2.60	0.51	1.60	0.14	−1.23	0.22

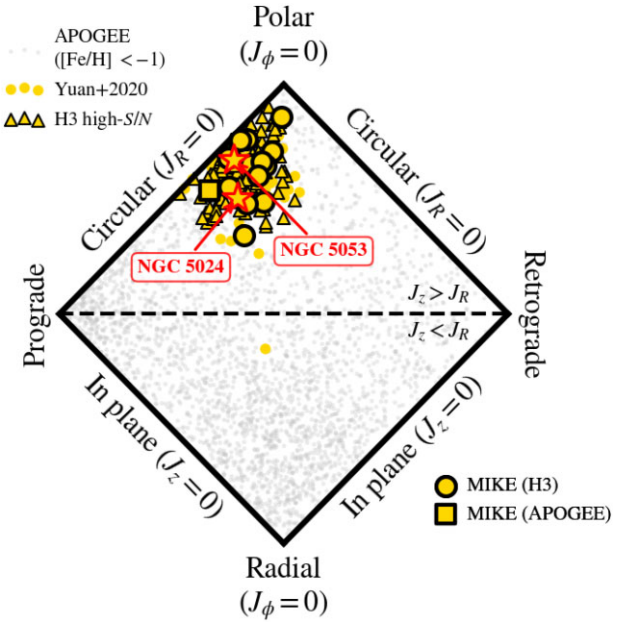

Figure 1. Wukong/LMS-1 stars in projected action-space diagram. The horizontal axis corresponds to J_ϕ/J_{total}, where $J_{total} = J_R + |J_\phi| + J_z$ (see the text). The vertical axis is $(J_z - J_R)/J_{total}$. Larger symbols with thick edges are those observed with MIKE; circles for H3 targets (Wuk_1 through _13) and square for the APOGEE one (Wuk_14). Triangles with thin edges are the 'high-*S/N*' sample of Wukong/LMS-1 members from Johnson et al. (2022). Smaller circles without edges are the 'LMS-1' stars from Yuan et al. (2020, see the text). Small dots in the background are metal-poor ([Fe/H] < −1) stars from APOGEE DR17. Star symbols are the Wukong/LMS-1 globular clusters NGC 5024 (M53) and NGC 5053.

5053, all phase-space information is from Vasiliev & Baumgardt (2021). We realized each orbit 100 times in a Monte Carlo scheme assuming Gaussian uncertainties for these quantities. The final adopted values are the medians of the resulting distributions. The adopted distance from the Sun to the Galactic centre is 8.2 kpc (Bland-Hawthorn & Gerhard 2016), the circular velocity at this position is 232.8 $km\,s^{-1}$ (McMillan 2017), and the assumed peculiar motion of the Sun is $(U, V, W)_\odot = (11.10, 12.24, 7.25)$ $km\,s^{-1}$ (Schönrich, Binney & Dehnen 2010).

We note that the model potential as well as Galactic fundamental parameters adopted here are different from previous H3 survey works (Naidu et al. 2020; Johnson et al. 2022). Therefore, the criteria used by these authors to select Wukong/LMS-1 stars become slightly different after our above-described calculations. In the spirit of making this paper self-sufficient, we provide updated values for the kinematic/dynamical quantities that define the Wukong/LMS-1 structure below. Nevertheless, we reinforce that the original target selection was made simply based on the H3 survey samples from Naidu et al. (2020) and Johnson et al. (2022) plus covering the largest possible metallicity range within the available telescope allocation.

Following Johnson et al. (2022), we have:

(i) $(J_z - J_R)/J_{total} > 0.3$ [4] and
(ii) $90° < \theta < 120°$,

[4]We call the attention to the difference in definition of J_{total} between ours and Naidu et al.'s (2020) work, also Johnson et al. (2022). These authors assumed the vectorial definition $J_{total} = \sqrt{J_R^2 + J_\phi^2 + J_z^2}$.

where $J_{\rm total} = J_R + |J_\phi| + J_z$ (Fig. 1) and $\theta = \arccos(L_z/L)$ refers to the orbital inclination, which characterizes the direction of the angular momentum vector $\boldsymbol{L} = (L_x, L_y, L_z)$ in a Galactic Cartesian frame. Within these definitions, $L = \sqrt{L_x^2 + L_y^2 + L_z^2}$ is the total angular momentum and $L_z \equiv J_\phi$ is the vertical component of it, where $L_z < 0$ indicates prograde motion. These criteria are accompanied by those from Naidu et al. (2020):

(i) $-1000 < L_z/(\mathrm{kpc\,km\,s^{-1}}) < 0$ and
(ii) $E < -1.15 \times 10^5\,\mathrm{km^2\,s^{-2}}$,

where E is the total orbital energy. Apart from these cuts, Naidu et al. (2020) also removed possible Sagittarius stream interlopers using the simple method of Johnson et al. (2020), which has been shown to be likely complete (Peñarrubia & Petersen 2021). Hence, when selecting *for* Wukong/LMS-1, one can use

(i) $L_y > -2000\,\mathrm{kpc\,km\,s^{-1}}$,

fully eliminating Sagittarius contamination within its L_z range. Naidu et al. (2020) also included a cut in orbital eccentricity to eliminate GSE stars. However, this is redundant with the action-space selection of Johnson et al. (2022) that requires $J_z > J_R$.

We observed all the Wukong/LMS-1 stars with the Magellan Inamori Kyocera Echelle (MIKE; Bernstein et al. 2003) spectrograph installed in the Magellan Clay telescope (6.5 m) located at Las Campanas Observatory, Chile. For all stars over all observing runs (2022 June for H3 follow-up and 2023 May for APOGEE), we used 0.7 arcsec slit and 2 × 2 on-chip binning. This configuration leads to resolving powers of $\mathcal{R} \sim 35\,000$ and 28 000 for the blue (wavelength $\lambda < 5000$ Å) and red ($\lambda > 5000$ Å) arms of MIKE spectra, respectively. All data were reduced using the CARPY[5] package (Kelson 2003). The final *S/N* reached was typically 30–40 per pixel at 4500 Å and 50–70 at 6500 Å (Table 1).

2.2 Radial velocities and spectra normalization

We derived RVs for all Wukong/LMS-1 stars by cross-correlating against a high-*S/N* MIKE spectrum of the metal-poor standard HD 122 563 using the Labeling Echelle Spectra with SMHR and Payne (LESSPAYNE;[6] A. P. Ji, in preparation) code. In a nutshell, LESSPAYNE combines Spectroscopy Made Harder (SMHR;[7] Casey 2014) with PAYNE4MIKE[8] (Ting et al. 2019)[9] and consolidates it into a single package. As of now, the RV measurement routine within LESSPAYNE is a carbon-copy of SMHR's. The formal statistical uncertainty of RVs from MIKE spectra ('$\mathrm{RV_{MIKE}}$' in the top panel of Fig. 2 and Table 1) could, in principle, reach $\sim$0.1 km s^{-1}. However, a systematic error of $\sim$1 km s^{-1} is introduced due to slit centring and wavelength calibration (see discussion by Ji et al. 2020b). For the purpose of this work, we are satisfied that the membership of our stars does not depend on the choice of RV value, either MIKE or H3/APOGEE. Indeed, at this RV precision, distances are the dominant source of errors for orbital parameters. The maximum difference between our MIKE RVs and H3 ones is $\approx$10 km s^{-1} (Wuk_4), but is usually $<$2 km s^{-1} (Fig. 2). See Section 4.1 for the possibility that Wuk_4 is in a binary system. For the APOGEE star Wuk_14, the difference in RV is 0.5 km s^{-1}.

[5] https://code.obs.carnegiescience.edu/mike
[6] https://github.com/alexji/LESSPayne
[7] https://github.com/andycasey/smhr
[8] https://github.com/alexji/Payne4MIKE
[9] https://github.com/tingyuansen/Payne4MIKE

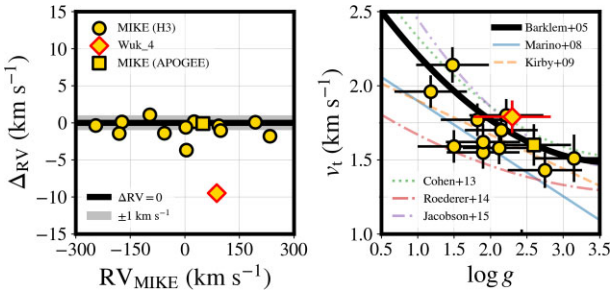

Figure 2. Left: comparison between MIKE and survey RVs, either H3 (circles and diamond) or APOGEE (square). The vertical axis shows $\Delta_{\rm RV}$, which corresponds to MIKE RVs minus H3/APOGEE ones. The black line shows $\Delta_{\rm RV} = 0$ and the shaded region covers $\pm$1 km s^{-1}, the systematic RV uncertainty for MIKE measurements. Right: log g versus $v_{\rm t}$ relation (see the text). Different lines are empirical quadratic fits to various samples of low-metallicity stars (Barklem et al. 2005; Marino et al. 2008; Kirby et al. 2009; Cohen et al. 2013; Roederer et al. 2014; Jacobson et al. 2015, see Ji et al. 2023a). The thickest line was used to determine the $v_{\rm t}$ for the most metal-poor star analysed (Wuk_6; see the text). Wuk_4 is shown as the diamond in both panels (see Section 4.1).

With the reduced data and RVs at hand, we proceed to stitch orders and normalize the MIKE spectra using cubic spline functions. LESSPAYNE initializes SMHR-like files from the best-fitting PAYNE4MIKE synthetic spectrum. This procedure drastically accelerates the normalization and equivalent width measurements, as it identifies where absorption features occur and masks them. This method is identical to the one described in Ji et al. (2023b), with the difference that, now, the whole process has been packaged into LESSPAYNE. The entire spectrum was inspected for all stars, but the LESSPAYNE continuum needed minor fixes only at the bluest orders, where *S/N* is lower, or when prominent wide absorption was present, such as Ca II K/H (3900–4000 Å) and/or the C-H *G* band ($\sim$4300 Å).

3 METHODS

For this project, we considered the atomic and molecular line list from Ji et al. (2020a), which was adapted from the LINEMAKE[10] compilation (Placco et al. 2021). This line list was also used by Ji et al. (2020a) to analyse the Indus and Jhelum streams that could be associated with Wukong/LMS-1 and which we compare to in Section 4. We rejected all lines at $<$3860 Å in our analysis due to the lower *S/N* at the bluest portions of the MIKE spectra. For our equivalent width measurements, we assumed Gaussian profiles. Lines that required Voigt profiles were rejected, with the exception of those in the Mg I triplet (5150–5200 Å). Abundances for Mg from these strong lines are consistent with others considered. Overall, we fitted between 70 (for our most metal-poor star) and 380 (most metal-rich) lines in each MIKE spectrum. Individual line measurements are provided in supplementary online tables.

3.1 Stellar parameters

We computed fully spectroscopic stellar parameters for all stars under the assumption of local thermodynamic equilibrium (LTE) using LESSPAYNE, which wraps the radiative transfer code MOOG (Sneden 1973), specifically a well-tested version[11] that includes appropriate

[10] https://github.com/vmplacco/linemake
[11] https://github.com/alexji/moog17scat

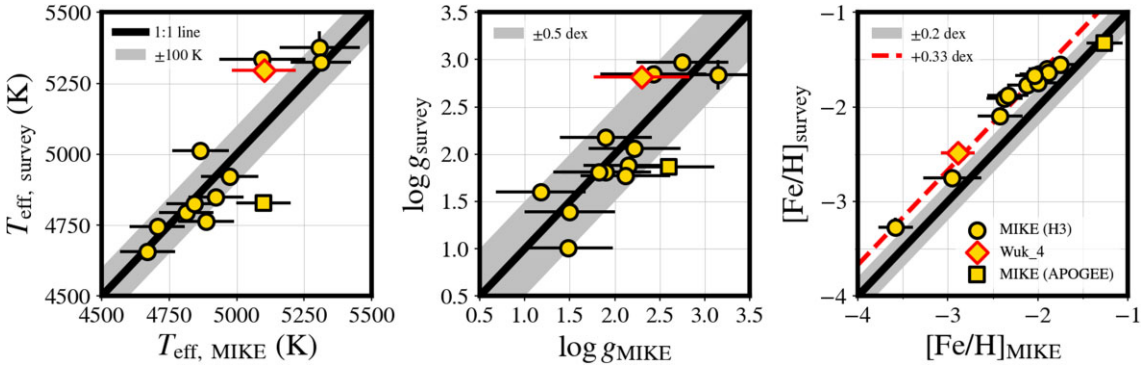

Figure 3. Comparisons between our derived stellar parameters from MIKE spectra (horizontal axes; Table 1) and the values from the spectroscopic surveys (vertical), either H3 (circles and diamond) or APOGEE (square). Left: $T_{\rm eff}$. Middle: log g. Right: [Fe/H]. One-to-one lines are shown in as thick solid lines. Shaded areas represent the systematic uncertainties adopted. The dashed line in the right panel shows the average difference between our derived metallicities and those from H3. Wuk_4 is shown as the diamond in all panels (see Section 4.1).

treatment of scattering (Sobeck et al. 2011). We employed α-enhanced ($[\alpha/{\rm Fe}] = +0.4$) 1D plane-parallel model atmospheres (Castelli & Kurucz 2003) in our analysis.

Effective temperatures ($T_{\rm eff}$) were estimated by balancing the abundances of Fe I lines against their excitation potential. Surface gravity values (log g) were found by minimizing the difference between Fe I and Fe II abundances. Microturbulence velocities ($v_{\rm t}$) were determined by reducing the trend between Fe II abundances and reduced equivalent widths; Fe II lines are preferred as they cover a wider range of reduced equivalent width values in red giants and are less affected by non-LTE (NLTE) effects (see Ji et al. 2020a). For the most metal-poor star in our sample (Wuk_6; model atmosphere metallicity [M/H] $= -3.57$), only three Fe II lines were available. Hence, for this star, we obtained $v_{\rm t}$ from the empirical relation with log g based on the work of Barklem et al. (2005, see appendix B of Ji et al. 2023a and bottom panel of Fig. 2).

Lastly, we recalibrated the $T_{\rm eff}$ for each star to the 'photometric scale' of Frebel et al. (2013) and, then, rederived log g and $v_{\rm t}$ by repeating the same steps described above. We reanalysed from scratch a couple of stars from Ji et al. (2020a) with our method and verified that these authors' photometric stellar parameters are compatible (1σ) with those revised with the Frebel et al. (2013) correction. On average, $T_{\rm eff}$ values become $\approx$200 K hotter after this step. For log g and [M/H], the corrected values are, on average, 0.67 dex and 0.24 dex larger, respectively. For $v_{\rm t}$, the final values are 0.07 km s^{-1} lower on average. Note that we do *not* just apply constant offsets, but rather the stellar parameters of each star change independently according to their recalibrated $T_{\rm eff}$ and these listed values are simply the average corrections. In Table 1 (also all figures), we provide only corrected parameters. Stellar parameters prior to recalibration are provided as online supplementary material. Throughout the remainder of this work, we consider only recalibrated stellar parameters, including for the abundance analysis (Section 3.2).

Apart from just statistical uncertainties, which come from the fitting process of individual lines as well as from the slopes of the excitation/ionization balance fits, it is crucial to consider systematics that can affect our stellar parameters and which are propagated into abundances. Systematic errors in stellar spectroscopic analysis come, in principle, from departures from the 1D LTE assumption, i.e. 3D and/or NLTE effects, which are especially relevant for metal-poor giants (Asplund 2005). In order to obtain empirically motivated systematic errors, we looked at the sample of low-metallicity stars analysed by Ezzeddine et al. (2020), which spans a wide range of stellar parameters that completely encompasses our sample; $4600 < T_{\rm eff}/{\rm K} \lesssim 5300$, $1 < \log g \lesssim 3$, $-3.50 \lesssim [{\rm Fe/H}] < -1.25$, and $1 < v_{\rm t}/({\rm km\,s^{-1}}) \lesssim 2$. These authors provided different sets of stellar parameters for each of their stars, including 1D LTE with the Frebel et al. (2013) correction and 1D NLTE. We verified that the average differences between these stellar parameter estimates are 100 K, 0.5 dex, 0.1 km s^{-1}, and 0.2 dex for $T_{\rm eff}$, log g, $v_{\rm t}$, and [Fe/H] and these values are adopted as systematic errors, summing in quadrature with the statistical ones to obtain final uncertainties for these quantities. For Wuk_6, we adopted a $v_{\rm t}$ statistical uncertainty of 0.12 km s^{-1}, which is the intrinsic scatter from the quadratic fit to the log g versus $v_{\rm t}$ relation. We note that, despite the apparently excessively large log g errors, $T_{\rm eff}$ continues to have the most important impact on abundance uncertainties.

A comparison between our MIKE parameters and those from the H3 survey/MINESWEEPER is provided in Fig. 3. For $T_{\rm eff}$ and log g, these are compatible (1σ) for all stars. For [Fe/H], H3 values are larger by $\sim$0.3 dex, but this level of systematics can be attributed to NLTE effects (see fig. 2 of Ezzeddine et al. 2020). In comparison to APOGEE parameters, we found $T_{\rm eff}$ and log g differences of $\sim$300 K and $\sim$0.7 dex, respectively, but with equivalent [Fe/H] values (also Fig. 3). We note, however, that, before applying the Frebel et al. (2013) photometric correction, our purely spectroscopic $T_{\rm eff}$ and log g would be compatible (1σ) with APOGEE values. With respect to the H3 values, this survey adopts spectrophotometric fits to obtain stellar parameters from broad-band photometry and model isochrones. Henceforth, it is not unexpected that our photometrically recalibrated $T_{\rm eff}$ and log g are similar, as is the case between ours and Ji et al.'s (2020a) photometric stellar parameters.

3.2 Abundances

We obtained abundances for up to 29 species of 24 elements. Equivalent widths were used for the abundances of Na I, Mg I, Si I, K I, Ca I, Ti I, Ti II, Cr I, Cr II, Ni I, Zn I, and Sr I, as well Fe I and Fe II. For heavily blended features, molecular features, or those requiring hyperfine splitting, we defaulted to spectral synthesis. For the task, LESSPAYNE performs a χ^2 minimization over local continuum with RV and abundance as free parameters, as well as a smoothing parameter to account for resolution. This approach was employed for C-H and C-N molecules, Al I, Sc II, V I, V II, Mn I, Co I, Sr II, Y II, Zr II, Ba II, La II, Eu II, and Dy II. We also synthesized the Si I

line at 3905 Å due to substantial blending. Additionally, we applied this technique to derive 5σ upper limits for O I, as well as other elements, for all our stars. For C-H and C-N, we adopted $^{12}C/^{13}C = 9$. For Ba and Eu, solar *r*-process isotopic ratios were assumed (Sneden, Cowan & Gallino 2008). For [Ti/Fe], [V/Fe], [Cr/Fe], and [Sr/Fe] ratios, we adopt Ti II, V I, Cr I, and Sr II as our fiducial values (Fig. 4).

Final abundances were calculated as inverse-variance weighted averages, taking into account uncertainties from individual lines for each species. Our adopted procedure is similar to Ji et al. (2020b), which neglects correlations between stellar parameters (McWilliam, Wallerstein & Mottini 2013). The one difference between our methodology and these authors' is the inclusion of an error floor on a line-by-line basis ($\sigma_{\rm sys}$), which should encapsulate additional unknowns coming from, for instance, atomic data or the 1D model atmospheres (see Ji et al. 2020a). For this purpose, we adopted a constant $\sigma_{\rm sys} = 0.1$ dex floor for most lines. For some species with hyperfine splitting, where the smoothing kernel might be degenerate with abundance, such as Sc, Mn, and Ba, we add an extra 0.1 dex, i.e. $\sigma_{\rm sys} = 0.2$ dex for all lines. For the C-N molecular band, which is located in the bluest part of MIKE spectra (3865–3885 Å) where the *S/N* is low and the continuum placement is difficult, we implemented $\sigma_{\rm sys} = 0.3$ dex. The Al line at 3961 Å, which is the only one considered for this element, not only suffers from the same caveats as the C-N, but is also at the wing of a hydrogen line (Hϵ), so we employed $\sigma_{\rm sys} = 0.3$ dex for it as well. We provide the relevant equations below, which are analogous to equations 1 to 5 in Ji et al. (2020b), but incorporating our modification and with updated terminology.

For a certain line *i* of a given element/specie X, its total uncertainty (σ_i) of the associated abundance (A_i) can be written as the quadrature sum of the different sources of error, i.e.

$$\sigma_i^2 = \sigma_{i,\rm stat}^2 + \sigma_{i,\rm SP}^2 + \sigma_{i,\rm sys}^2, \tag{1}$$

where $\sigma_{i,\rm stat}$ is the statistical error, which comes from spectrum noise and the line-fitting procedure, and $\sigma_{\rm SP}$ is the total stellar-parameter error budget;

$$\sum_{\rm SP} \delta_{i,\rm SP}^2 = \sigma_{i,\rm SP}^2 = \delta_{i,T_{\rm eff}}^2 + \delta_{i,\log g}^2 + \delta_{i,v_{\rm t}}^2 + \delta_{i,\rm [M/H]}^2. \tag{2}$$

In this equation, $\delta_{i,T_{\rm eff}}$, $\delta_{i,\log g}$, $\delta_{i,v_{\rm t}}$, and $\delta_{\rm i,\,[M/H]}$ are abundance offsets associated with uncertainties in $T_{\rm eff}$, log g, $v_{\rm t}$, and [M/H], respectively, as listed in Table 1. Because these quantities retain their sign, we refer to them as '$\delta_{i,\,...}$'. Finally, the inverse-variance weights can be assigned to each line,

$$w_i = \frac{1}{\sigma_i^2}, \tag{3}$$

and the final abundance can be computed as

$$A({\rm X}) = \frac{\sum_i^N w_i A_i}{\sum_i^N w_i}, \tag{4}$$

where N is the total amount of lines available for X.

Uncertainties in A(X), as well as abundance ratios, are propagated in an identical fashion to Ji et al. (2020b). Again, to make this paper self-sufficient, we reproduce these authors' equations (6) through (10) (see their appendix) below.

$$\sigma_{\rm stat}^2 = \frac{\sum_i^N w_i [A_i - A({\rm X})]^2}{\sum_i^N w_i} + \frac{1}{\sum_i^N w_i}, \tag{5}$$

where this total statistical uncertainty for abundance A(X) includes the weighted standard error across abundances A_i for N different lines i of element/specie X as well as spectrum noise. Note that when $N = 1$, the first term of equation (5) goes to zero and, in that situation, the second term is fully responsible for propagating line-by-line errors (including our $\sigma_{\rm sys}$) to the final $\sigma_{\rm stat}$ through the weights pre-computed by equation (3). For stellar parameters,

$$\delta_{\rm SP} = \frac{\sum_i^N w_i \delta_{i,\rm SP}}{\sum_i^N w_i}. \tag{6}$$

We recall that covariance between stellar parameters ($T_{\rm eff}$, log g, v_t, and [M/H]) is neglected (see McWilliam et al. 2013). Then, the total error budget for an abundance ratio [X/H] between element/specie X and hydrogen is obtained by summing statistical and stellar-parameter uncertainties in quadrature:

$$\sigma_{\rm [X/H]}^2 = \sigma_{\rm stat}^2 + \sum_{\rm SP} \delta_{\rm SP}^2. \tag{7}$$

Finally, the uncertainty of an abundance ratio between elements/species X and Y accounts for covariance between X and Y through stellar parameters:

$$\sigma_{\rm [X/Y]}^2 = \sigma_{\rm X,stat}^2 + \sigma_{\rm Y,stat}^2 + \sum_{\rm SP} (\delta_{\rm X,SP} - \delta_{\rm Y,SP})^2. \tag{8}$$

Our abundance inventory is shown in Fig. 4. Our Wukong/LMS-1 stars (yellow symbols) are plotted against a compilation of metal-poor stars (grey dots) from the Stellar Abundances for Galactic Archaeology (SAGA) data base (Suda et al. 2008, 2017), including the works of Fulbright (2000), Barklem et al. (2005), Cohen et al. (2013), Yong et al. (2013), Roederer et al. (2014), Jacobson et al. (2015), and Li et al. (2022). All abundance information, both ours and SAGA's, was normalized to the solar composition of Asplund et al. (2009). Whenever we mention the ratio between an element X and Fe ([X/Fe]), we adopt Fe I as reference. We highlight the red dashed line in the upper left panel of Fig. 4, which delineates the boundary for 'carbon-enhanced metal-poor' stars (CEMP; [C/Fe] $> +0.7$ and [Fe/H] < -1; Beers & Christlieb 2005, Aoki et al. 2007, Frebel & Norris 2015, Frebel 2018). Dotted lines portray the solar-level abundances ([X/Fe] = 0) in all panels.

4 RESULTS

Throughout this section, we compare our derived abundance information for Wukong/LMS-1 with literature results, also with the aid of SAGA data base (Suda et al. 2008, 2017), but not limited to, for other dwarf galaxies, accreted substructures, and stellar streams. We gathered data for three dSph galaxies, namely Sculptor (Scl; Shetrone et al. 2003; Geisler et al. 2005; Jablonka et al. 2015; Simon et al. 2015; Hill et al. 2019), Fornax (Fnx; Shetrone et al. 2003; Letarte et al. 2010), and Draco (Dra; Shetrone, Côté & Sargent 2001; Cohen & Huang 2009; Tsujimoto et al. 2015). We also consider Sagittarius (Sgr) dSph+stream (Hayes et al. 2020, updated to APOGEE DR17). We also took data for Reticulum II (Ret II; Ji et al. 2016a, b) ultra-faint dwarf (UFD). We adopt the sample of 'low-α' stars from Nissen & Schuster (2010, 2011), representing GSE, as an example of phase-mixed accreted dwarf.

For Indus and Jhelum stellar streams, we use the line measurements from Ji et al. (2020a), but we recomputed the average abundance ratios using our described methodology (Section 3.2) rather than the weights from their paper. We proceed into this section with the assumption that our analysed abundances for Wukong/LMS-1, Indus, and Jhelum are on a consistent scale and with the understanding that these stellar streams are all associated through a common progenitor dwarf galaxy. If these hy-

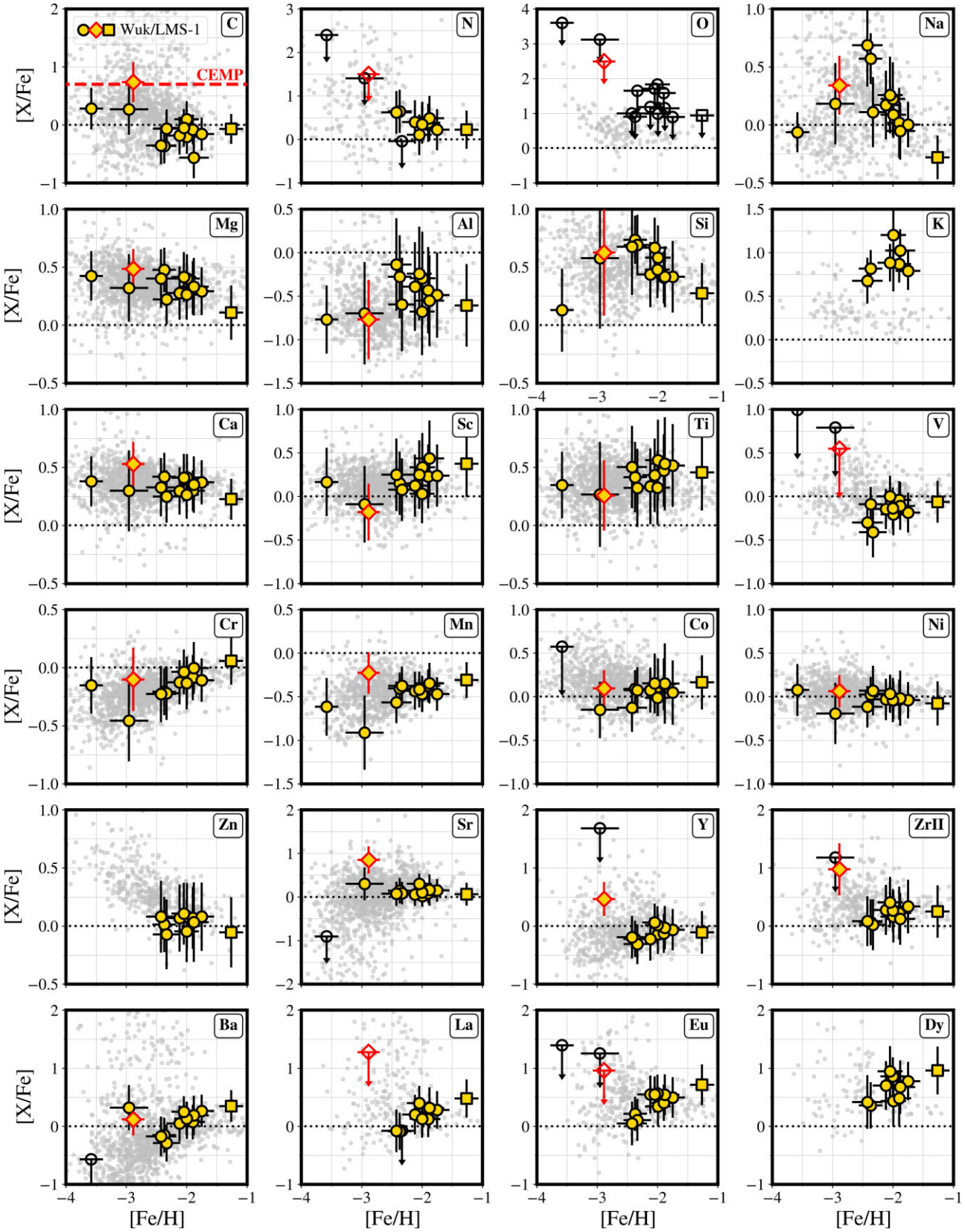

Figure 4. [X/Fe] versus [Fe/H] plots for all elements estimated in this work for our Wukong/LMS-1. In this figure, Fe is always Fe I. The top right corner of each panel shows the X element represented. Filled symbols are measured abundances, while open ones are upper limits. Circles and diamond correspond to stars followed-up from H3 (Wuk_1 to _13) and the square is from APOGEE (Wuk_14). Dotted lines at [X/Fe] = 0 show the solar level. The dashed line at [C/Fe] = +0.7 in the top left panel delineates the boundary for the definition of CEMP star (see the text). The diamond symbol is Wuk_4. In all panels, the dots in the background are metal-poor stars from our SAGA data base compilation (see the text).

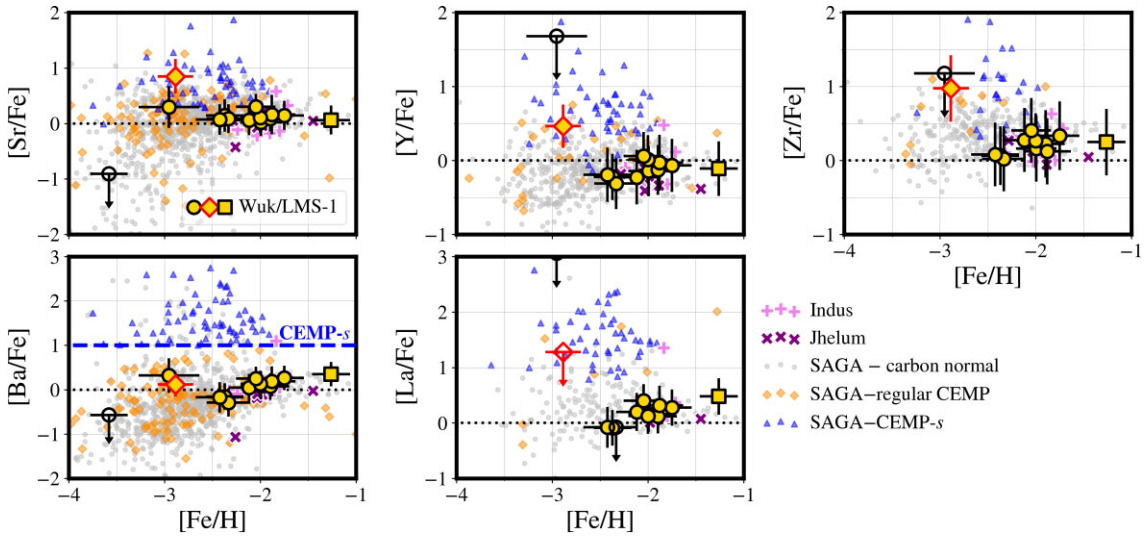

Figure 5. Abundance plots for some neutron-capture elements: [Sr, Y, Zr, Ba, La/Fe] versus [Fe/H]. Symbols with thick edges are our Wukong/LMS-1 stars with detected abundance for the given element in each panel. Empty symbols are upper limits. The diamond marker represents the CEMP star in our sample (Wuk_4). The square is the metal-rich star from APOGEE (Wuk_14). Indus and Jhelum stellar streams are shown as '+'+ and 'X' symbols, respectively. Small dots in the background are the metal-poor stars from the SAGA data base compilation with normal carbon enrichment ([C/Fe] $\leq +0.7$). Regular CEMP stars are marked as small diamonds ([C/Fe] $> +0.7$ and [Ba/Fe] $\leq +1.0$). CEMP-*s* stars ([C/Fe] $> +0.7$ and [Ba/Fe] $> +1.0$) are shown in small triangles (see dashed line in the bottom left panel). The solar abundance level is shown as dotted lines in all panels.

potheses hold true, the bulk of their chemical-abundance patterns should be effectively indistinguishable from each other. Having said that, we caution that, although chemistry is a great tool for falsifying associations between substructures, similar abundance patterns do not automatically confirm common origins, especially if these are not too different from the underlying halo population.

4.1 A CEMP star with peculiar neutron-capture signatures

It has been known for at least a couple of decades that the fraction of CEMP stars increase as function of decreasing metallicity (Beers, Preston & Shectman 1992; Norris, Ryan & Beers 1997; Rossi, Beers & Sneden 1999; Rossi et al. 2005; Lucatello et al. 2006; Lee et al. 2013; Placco et al. 2014, 2018; Yoon et al. 2018, and see Arentsen et al. 2022 for a compilation). The evolution of the CEMP fraction with [Fe/H] appears to be identical between the Milky Way's halo and UFD galaxies (Ji et al. 2020b). However, detailed studies for some more massive dwarfs, such as classical dSph ones, show that some discrepancy might exist with the Milky Way, in particular for Sculptor (Skúladóttir et al. 2015; Chiti et al. 2018; Skúladóttir et al. 2021, 2024) and, possibly, Sagittarius (Chiti & Frebel 2019; Chiti, Hansen & Frebel 2020, but see Limberg et al. 2023).

In this context, we confirm that Wuk_4, one of our most metal-poor Wukong/LMS-1 members ([Fe/H] $= -2.89 \pm 0.19$), is a CEMP star ([C/Fe] $= +0.74 \pm 0.25$; top left panel of Fig. 4, symbol with red edge). The carbon-abundance correction for evolutionary effects is only $+0.01$ dex (Placco et al. 2014). After, applying the carbon correction to all other stars in our Wukong/LMS-1 sample, none of them turned out to be CEMP. The corrected [C/Fe] values for all stars are provided alongside the full abundance table as supplementary material. Wuk_4 had already been identified as a CEMP candidate by Lucey et al. (2023) through spectrophotometric data from *Gaia* DR3. Wuk_4 also shows strong enhancement in Sr, Y, and Zr ($+0.5 \lesssim$ [X/Fe] $\leq +1.0$; upper panels of Fig. 5). Interestingly, this is not accompanied by significant enrichment in either Ba ([Ba/Fe] $= +0.12 \pm 0.24$) or La (only upper limit found) as would be expected if Wuk_4 was a 'typical' CEMP-*s* star (Beers & Christlieb 2005; Frebel 2018), i.e. a CEMP star also enhanced in the slow (*s*-) neutron capture process (defined as [Ba/Fe] $> +1.0$). Apart from Wuk_4, other Wukong/LMS-1 stars have effectively identical chemical compositions to the bulk of Indus and Jhelum stars in all abundance panels in Fig. 5 (Sr, Y, Zr, Ba, La).

In Fig. 5, we exhibit the same SAGA data base low-metallicity compilation from Fig. 4, but, now, dividing into carbon-normal (grey points), regular CEMP (orange diamonds), and CEMP-*s* (blue triangles) stars. From the top panels, it becomes clear that CEMP-*s* stars are also preferentially enhanced in Sr, Y, and Zr. Nevertheless, there are a few examples of ordinary CEMP stars with high values of [Sr/Fe], [Y/Fe], and/or [Zr/Fe] similar to Wuk_4. In any case, it is also rather suspicious that Wuk_4 is the only star with significant ($\approx$10 km s^{-1}, $\gtrsim 5\sigma$) RV difference between H3's and our measurement (Section 2.2), possibly indicating a binary system. Indeed, binarity is believed to be the conventional pathway for the formation of CEMP-*s* stars as they would experience mass transfer from an asymptotic giant branch companion (e.g. Lucatello et al. 2005; Hansen et al. 2016 for RV monitoring studies and Travaglio et al. 2004 for nucleosynthesis). Nevertheless, CEMP-no stars, those without any signatures of *s*-process enhancement ([Ba/Fe] < 0.0) are also, sometimes, found in long period binaries (Arentsen et al. 2019; Bonifacio et al. 2020). Deciphering whether or not mass transfer in a binary can create the excess of Sr, Y, and Zr in Wuk_4 without high Ba will demand a systematic investigation of other CEMP stars with similar abundance patterns in the future.

4.2 α elements reveal a relatively massive dwarf galaxy

Now, we look at the [α/Fe] ratios in Wukong/LMS-1 stars, specifically the abundances of Mg and Ca. We only derived upper limits for

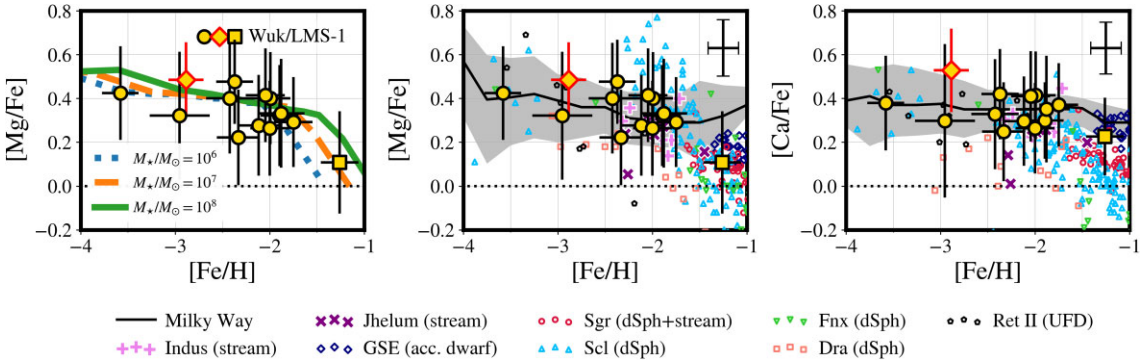

Figure 6. Abundance trends of α-elements Mg (left and middle) and Ca (right) in [α/Fe] versus [Fe/H] format. Symbols with thick edges are our Wukong/LMS-1 stars. The diamond represents the CEMP star in our sample (Wuk_4). The square is the most metal-rich star followed-up from APOGEE (Wuk_14). Indus and Jhelum stellar streams are shown as '+' and 'X' symbols, respectively. In the left panel, dotted, dashed, and solid lines are chemical evolution trajectories for galaxies with stellar masses $M_\star/M_\odot$ of 10^6, 10^7, and 10^8, respectively (Wanajo et al. 2021, see the text). In the middle and right panels, the solid line shows the median abundances from the SAGA data base compilation of metal-poor stars in bins of 0.25 dex in [Fe/H]. The shaded band represents 16th and 84th percentiles within the same bins. Stars from Sagittarius (Sgr), Sculptor (Scl), Fornax (Fnx), and Draco (Dra) dSph galaxies, Reticulum II (Ret II) UFD, as well as GSE disrupted dwarf, are exhibited for comparison. See the text for details on our abundance compilation for these dwarf galaxies. The solar abundance level is shown as dotted line in all panels. The error bars in the top right corner of the middle and right panels show statistical uncertainties alone in [Mg/Fe] and [Ca/Fe], respectively, as well as [Fe/H].

O and Si is less reliable than Mg and Ca in the low-metallicity regime (see discussion in Ji et al. 2020a). The behaviour of α abundances is a great tracer of the overall star-formation history of a galaxy (Tinsley 1979; Matteucci 2012). More massive systems are expected to enrich themselves (i.e. reach higher metallicities) via core-collapse supernovae before the occurrence of Type Ia supernovae, which is delayed by $\gtrsim$100 Myr (e.g. Maoz & Mannucci 2012; de los Reyes et al. 2022). Because core-collapse supernovae produces mostly α elements while the Type Ia create almost exclusively iron-peak elements (for a review, see Nomoto, Kobayashi & Tominaga 2013), a characteristic downturn in [α/Fe] is expected at a certain metallicity (referred to as the 'knee'; Matteucci & Greggio 1986). The location of this knee in [Fe/H] depends on the star-formation and outflow efficiency, hence the mass, of a given galaxy (e.g. Matteucci & Brocato 1990; Tolstoy et al. 2009). This is illustrated in Fig. 6 (left panel) by the simulated chemical-evolution trajectories of Wanajo, Hirai & Prantzos (2021, their fig. 4, case 1) for dwarf galaxies with different stellar masses ($10^6 \leq M_\star/M_\odot \leq 10^8$) at redshift $z = 0$, similar to canonical dSph Milky Way satellites and encompassing the expected value for Wukong/LMS-1's progenitor. We note that we subtracted 0.25 dex from their model's [Mg/H] values so the 'plateau' is positioned at about +0.4 dex. These recalibrated versions of the models will also be used in Section 4.4.

In Wukong/LMS-1, our derived abundances of both Mg and Ca reveal that the [α/Fe] ratio remains high ($\sim$0.3–0.4 dex) up to [Fe/H] $\gtrsim -2$ (Fig. 6). This is, indeed, similar to somewhat massive surviving Milky Way satellites (Kirby et al. 2011; Reichert et al. 2020). Before our analysis, the evidence for Wukong/LMS-1's progenitor being a relatively massive dwarf ($M_\star \sim 10^7\,M_\odot$) came from tentative dynamical N-body modelling (Malhan et al. 2021), the scaling relation between the total mass of its globular clusters and a galaxy's mass (also Malhan et al. 2021), or simple star counts (Naidu et al. 2022). Hence, we provide the first evidence in favour of this hypothesis from chemistry. An identical α-element abundance pattern is seen in Indus and Jhelum (pink and purple crosses, respectively, in Fig. 5 and beyond; Ji et al. 2020a). As previously mentioned, although this chemical similarity between these streams does not fully confirm their association, it still corroborates such scenario.

Although the models in Fig. 6 exemplify how a galaxy's mass correlates with its chemical evolution, we do not claim to be actually measuring the stellar mass of Wukong/LMS-1 from abundances. Systematics make the uncertainties of our [Mg/Fe] and [Ca/Fe] estimates to be typically 0.2 dex. For reference, the median statistical uncertainties are $\approx$0.1 dex for these [α/Fe] ratios (top right corner in middle and right panels of Fig. 6). Not only this precision does not allow us to differentiate between those models, but the models themselves carry potentially even worse systematics such as supernovae and/or NSM yields. Nevertheless, we reinforce that the constant, within errors, [α/Fe] up to [Fe/H] ~ -2 is in conformity with the behaviour seen in the *data* of nearby massive ($M_\star/M_\odot \geq 10^6$) dwarfs.

It is also relevant that the most metal-rich star ([Fe/H] $= -1.26 \pm 0.20$, Wuk_14; yellow square in all figures) in the sample has lower [Mg/Fe] and [Ca/Fe] than the bulk of our observed Wukong/LMS-1 members ([Fe/H] ≤ -1.75) by 0.1–0.2 dex (middle and right panels of Fig. 6). This is, perhaps, not a particularly surprising result given that we observed this additional star specifically with the goal of testing the standard chemical enrichment scenario as discussed above. Nevertheless, we notice that Jhelum also contains a low-α star at [Fe/H] $= -1.45$, which adds to the emerging picture where Wukong/LMS-1 progenitor experienced quite a simple chemical evolution pathway. It is also informative that Wukong/LMS-1 shows no evidence for additional bursts of star formation, which would cause the [α/Fe] to actually increase at higher [Fe/H], a phenomenon that happens to some dwarfs, such as Sagittarius, Fornax, and the Magellanic Clouds (see Nidever et al. 2020; Hasselquist et al. 2021), and is expected to be caused by their interaction with their massive host (in this case, the Milky Way). We did not find any trustworthy Wukong/LMS-1 candidates at metallicities higher than Wuk_14 neither in H3 nor in APOGEE.

4.3 A pair of stars with abundances reminiscent of multiple stellar populations in globular clusters

Almost all globular clusters are known to contain more than just a single, sometimes several, well-defined sequences in optical/ultraviolet colour–magnitude diagrams (Piotto et al. 2015; Milone et al. 2017).

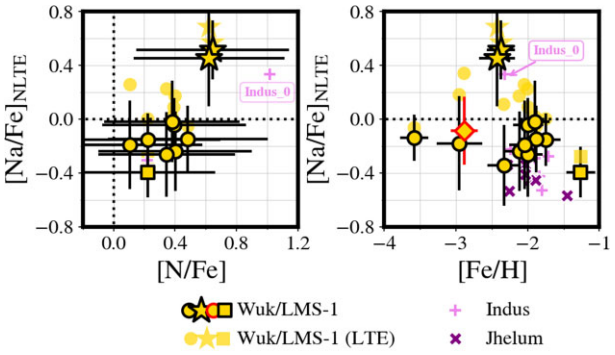

Figure 7. Left: $[Na/Fe]_{NLTE}$ versus [N/Fe]. Right: $[Na/Fe]_{NLTE}$ versus [Fe/H]. In both panels, $[Na/Fe]_{NLTE}$ represents our sodium-to-iron ratios corrected with the NLTE departures from Lind et al. (2011, see the text). Symbols with thick edges are Wukong/LMS-1 stars in our sample. The diamond represents the CEMP star in our sample (Wuk_4). The square is the most metal-rich star followed-up from APOGEE (Wuk_14). Star symbols represent the N-/Na-rich stars (Wuk_5 and Wuk_11). Symbols without edges in the background correspond the same Wukong/LMS-1 stars, but without the NLTE corrections to Na. Indus and Jhelum stellar streams are shown as '+' and 'X' symbols, respectively. Indus_0, which is also N-/Na-rich (see the text), is tagged in both panels. The solar abundance level is shown as dotted lines in both panels.

Colour differences between these distinct tracks are caused by star-to-star variations in their abundances of light elements, including correlated enhancements in N and Na (e.g. Gratton, Sneden & Carretta 2004). Such phenomenon is referred to as 'multiple stellar populations' (Bastian & Lardo 2018; Milone & Marino 2022). Star clusters with multiple stellar populations have been detected not only in the Milky Way, but also other galaxies in the Local Group, including the Magellanic Clouds (Mucciarelli et al. 2009; Dalessandro et al. 2016) and even Fornax dSph (Larsen et al. 2014). Most recently, evidence has been provided for multiple stellar populations in globular-cluster stellar streams (Balbinot, Cabrera-Ziri & Lardo 2022; Martin et al. 2022; Usman et al. 2024). Interestingly, a clear detection of a N-/Na-rich star was actually first made in Indus (Ji et al. 2020a), which holds even after NLTE corrections to Na (Hansen et al. 2021).

Wukong/LMS-1 contains an additional pair of N-/Na-rich stars (top panel of Fig. 7), reinforcing the idea that its progenitor dwarf galaxy had not only NGC 5024 and NGC 5053 as globular clusters, but also at least one other that has been fully disrupted (Hansen et al. 2021), which is not unexpected for its mass (Eadie, Harris & Springford 2022). In order to guarantee that this result is robust against NLTE effects, we performed corrections following Lind et al. (2011). In practice, we corrected Na abundances line by line and, then, recomputed the weighted averages using our formalism (Section 3.2). In this process, uncertainties and weights remain unchanged. For consistency, we applied the same approach to both Indus and Jhelum stars. As can be appreciated from Fig. 7, NLTE corrections to Na exacerbate the differences between the bulk of our Wukong/LMS-1 members and its enriched stars; original LTE abundances are plotted in the background as transparent symbols. We note that both NGC 5024 and NGC 5053 are also very metal-poor ([Fe/H] $\lesssim -2$; Kruijssen et al. 2019 and references therein) and contain multiple stellar populations (see their ultraviolet colour–magnitude diagrams in Piotto et al. 2015)

From the bottom panel of Fig. 7, it is intriguing that both of our N-/Na-rich Wukong/LMS-1 stars (Wuk_5 at [Fe/H] $= -2.42 \pm 0.25$ and Wuk_11 at [Fe/H] $= -2.37 \pm 0.20$) have metallicities compatible (1σ) to their analogue in Indus (Indus_0; [Fe/H] $= -2.32 \pm 0.22$). We speculate that this could indicate that all these stars originated from a single disrupted globular cluster, though there is still not enough evidence to make a clear association. Nevertheless, if more stars at this metallicity of $\approx -$ 2.4 dex are found to have excess of N and Na in Indus, Jhelum, and the large Wukong/LMS-1, the scenario where they all belonged to the same, now completely disrupted, globular cluster would be reinforced. Furthermore, this underscores the exciting possibility of identifying more enriched globular-cluster stars embedded within other dwarf-galaxy streams, which would be further evidence in favour of the multiple stellar populations phenomenon being ubiquitous across different environments.

Now that we have strong indication that Wukong/LMS-1 had $\geq$3 globular clusters, we can utilize this information as independent constraint on the total mass of this dwarf (e.g. Forbes 2020; Callingham et al. 2022). We employ the relationship between the total number of globular clusters in a galaxy and its halo virial mass from Burkert & Forbes (2020, their equation 1). This exercise gives a total mass of $\approx 10^{10}\,M_{\odot}$ for Wukong/LMS-1. This value, indeed, translates into a stellar mass of $\sim 10^{7}$ assuming the stellar-to-halo mass relation from Rodríguez-Puebla et al. (2017) at redshift $z = 1$ ($\sim$8 Gyr ago in Planck Collaboration VI 2020 cosmology), consistent with expectations for Wukong/LMS-1 (Malhan et al. 2021; Naidu et al. 2022). From this line of reasoning, Wukong/LMS-1 might have contributed with $\sim$1 per cent of the present-day total mass of the Milky Way (e.g. Bland-Hawthorn & Gerhard 2016).

4.4 The rise of the *r*-process in Wukong/LMS-1

Finally, we look at the abundance patterns of rapid (*r*-) neutron capture process elements in Wukong/LMS-1. In 2017, the electromagnetic counterpart of the neutron-star merger (NSM) event GW170817 (Abbott et al. 2017a, b, c) provided confirmation that this site is capable of producing copious amounts of heavy elements via the *r*-process (Drout et al. 2017; Kilpatrick et al. 2017; Shappee et al. 2017). Notwithstanding, although NSMs could be the *only* site for the *r*-process, evidence has been presented that additional sources are involved (see the review by Cowan et al. 2021), in particular a prompt source might be needed to explain the full abundance patterns of both the Milky Way (Côté et al. 2019; Haynes & Kobayashi 2019; Kobayashi, Karakas & Lugaro 2020; Tsujimoto 2021) and some of its dSph satellites (Skúladóttir et al. 2019; Reichert et al. 2020; Skúladóttir & Salvadori 2020). The time-scales for *r*-process enrichment embedded into the chemical abundances of stars hold clues to its dominant astrophysical site(s).

As can be seen in the top panel of Fig. 8, the [Eu/Fe] ratio, where Eu is mostly produced by the *r*-process (see Sneden et al. 2008), increases from $<+$ 0.1 dex at [Fe/H] ~ -2.4 all the way up to $>+$ 0.7 dex at [Fe/H] ~ -1.3. The [Ba/Eu] ratio of Wukong/LMS-1 stars is effectively constant at $\sim-$ 0.4 dex, confirming that the production of these elements is dominated by the *r*-process. For reference, a 'pure' *r*-process signature is close to [Ba/Eu] $= -0.8$ (e.g. Bisterzo et al. 2014). These abundances overlap with both Indus and Jhelum, although the data for these other stellar streams do not cover as large of a metallicity interval. We also recall the existence of the extremely *r*-process rich star Indus_13 (Hansen et al. 2021), which is labelled in Fig. 8. The previously mentioned Wanajo et al. (2021) chemical-evolution sequences (Section 4.2) are plotted in the background of Fig. 8. These models contain *r*-process production exclusively from NSMs. The current data for Wukong/LMS-1 seems compatible with this scenario, without the need for a prompt source (such as core-

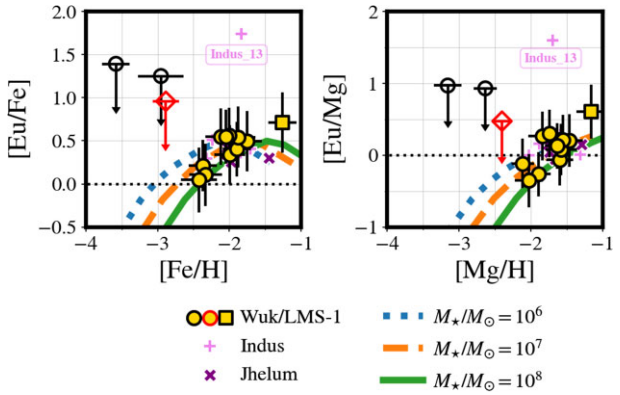

Figure 8. Left: [Eu/Fe] versus [Fe/H]. Right: [Eu/Mg] versus [Mg/H]. Symbols with thick edges are Wukong/LMS-1 stars in our sample. Empty symbols are upper limits. The diamond represents the CEMP star in our sample (Wuk_4). The square is the most metal-rich star followed-up from APOGEE (Wuk_14). Indus and Jhelum stellar streams are shown as '+' and 'X' symbols, respectively. Indus_13, which is an extremely *r*-process enhanced star is tagged in the top panel. In both panels, dotted, dashed, and solid lines are chemical evolution trajectories for galaxies with stellar masses $M_\star/M_\odot$ of 10^6, 10^7, and 10^8, respectively (Wanajo et al. 2021, see the text). The solar abundance level is shown as dotted line in both panels.

collapse supernovae) where [Eu/Fe] (or [Eu/Mg] as in the bottom panel of Fig. 8) would be constant over the low-metallicity regime. Note that we do not claim that NSMs are the only source of *r*-process in Wukong, but rather the dominant one within the metallicity range probed by our current data.

An increasing trend of [Eu/Fe] with [Fe/H] has also been claimed to exist in UMi dSph (Cohen & Huang 2010). However, this behaviour is accompanied by a huge scatter, which suggests that UMi actually experiences stochastic *r*-process enrichment, which, indeed, would be in line with its lower stellar mass ($M_\star \sim 10^5\,M_\odot$) in comparison to Sculptor, Fornax, and Sagittarius dSph galaxies ($M_\star > 10^6\,M_\odot$). Similar observations have also been made in another dwarf-galaxy stellar stream, the so-called 'Typhon' (Tenachi et al. 2022; Dodd et al. 2023, and Ji et al. 2023b for abundances). Nevertheless, the available data for that stream covers a shorter metallicity interval and the differences in [Eu/Fe] are smaller than in Wukong/LMS-1. Also, in Typhon, this result depends on a single star at [Fe/H] < -2. Therefore, Wukong/LMS-1 constitutes the first example of a dwarf galaxy, though in the form of a stellar stream, with *r*-process enrichment that is clearly dominated by delayed sources, presumably NSMs. Of course, additional measurements of Eu at lower metallicities ([Fe/H] < -2.5) will be necessary to test for the presence of a prompt *r*-process source in Wukong/LMS-1. Unfortunately, all stars analysed in this work at such low-metallicity regime are relatively hot ($T_{\rm eff} \gtrsim 5100$ K; Table 1, Wuk_4, 6, and 7), which impedes us from obtaining detections of Eu with the lines considered (4129 Å, 4205 Å, 4435 Å, 4522 Å, and 6645 Å).

5 CONCLUSIONS

We presented results from the first spectroscopic follow-up campaign for stars in the Wukong/LMS-1 dwarf-galaxy stellar stream with the Magellan Clay/MIKE combination. These targets were originally identified as members from the H3 (Naidu et al. 2020; Johnson et al. 2022) or APOGEE (Section 2.1) surveys. From these high-resolution MIKE spectra, we obtained RVs, stellar parameters, and detailed chemical abundances for 14 stars in Wukong/LMS-1 covering an extensive metallicity range ($-3.5 <$ [Fe/H] $\lesssim -1.3$). We also recalculated average abundances for a pair of stellar streams, Indus and Jhelum (Ji et al. 2020a), which have been suggested to be associated with the larger Wukong/LMS-1 (Bonaca et al. 2021; Malhan et al. 2021, 2022), in order to guarantee a consistent scale across samples. Our main results are summarized below.

(i) Wukong/LMS-1 is chemically indistinguishable from Indus and Jhelum. Although this is not enough to confirm that they originated in the same parent dwarf galaxy, this is certainly evidence in favour of this hypothesis.

(ii) We confirmed a CEMP star in Wukong/LMS-1 (Wuk_4; [Fe/H] $= -2.89 \pm 0.19$ and [C/Fe] $= +0.74 \pm 0.25$) with evidence for RV variation ($>5\sigma$ level) as well as peculiar enhancements ($+0.5 \lesssim$ [X/Fe] $\leq +1.0$) in Sr, Y, and Zr, which is reminiscent of the CEMP-*s* class, but without the expected high [Ba/Fe] ratio.

(iii) The [α/Fe] ratios (Mg, Ca) in Wukong/LMS-1 remain high ($\sim$0.3–0.4 dex) up to [Fe/H] $\gtrsim -2$, which is similar to relatively massive surviving dSph satellites of the Milky Way. This is in conformity with other works in the literature that estimated the mass of Wukong/LMS-1's progenitor with other methods (Malhan et al. 2021; Naidu et al. 2022). Moreover, the most metal-rich star in our sample (Wuk_14; [Fe/H] $= -1.26 \pm 0.20$), as well as a Jhelum star at -1.45 dex, has lower [α/Fe] by 0.1–0.2 dex in comparison to the bulk of Wukong/LMS-1 stars, suggesting that this dwarf galaxy likely experienced fairly standard chemical evolution.

(iv) Wukong/LMS-1 contains a pair of stars (Wuk_5 and Wuk_11) that are both N- and Na-rich in comparison to the bulk of the sample, which is a telltale sign that that these were born in a globular cluster with multiple stellar populations. This favours the hypothesis that Wukong/LMS-1 likely contained at least one globular cluster that has been completely disrupted. Interestingly, both of these Wukong/LMS-1 members plus a previously known N-/Na-rich Indus star all have compatible (1σ) metallicities ([Fe/H] $\equiv 2.4$).

(v) Because Wukong/LMS-1 is also associated with a couple of intact globular clusters, NGC 5024 (M53) and NGC 5053, plus the disrupted one, we used this information to estimate the halo virial mass of the progenitor system. For $\geq$3 globular clusters, a galaxy is expected to have a total mass of $\approx 10^{10}$, which corresponds to $\sim$1 per cent of the present-day Milky Way.

(vi) The [Eu/Fe] ratio in Wukong/LMS-1 stars increases as a function of metallicity within $-2.5 <$ [Fe/H] $\lesssim -1.3$, which can be reproduced by chemical-evolution models for similarly massive dwarfs with NSMs as the only source for the *r*-process (Wanajo et al. 2021), i.e. without the need for a prompt source. Wukong/LMS-1 is, in this context, the first example of dwarf galaxy with *r*-process enrichment clearly dominated by delayed sources.

This paper provides a powerful demonstration of how detailed abundances can be used to unveil the evolution of disrupted dwarf galaxies, which, given their low masses and high accretion redshift, cannot be spatially resolved, or detected (depending on the exact redshift), even by *JWST*. The combination between *Gaia* and complementary spectroscopic surveys can be employed to confidently identify members of streams/substructures if one is well-informed regarding potential interlopers, in particular from GSE and Sagittarius stream. We envision that the next step for Galactic archaeology will be to obtain samples covering larger metallicity ranges for these streams/substructures. Towards the low-metallicity regime, the number of available targets drastically diminishes. In the metal-rich end, Milky Way's halo foreground contamination is difficult to deal with. Therefore, dedicated searches for these targets

will be necessary for us to continue advancing our knowledge about the fundamental building blocks of our Galaxy.

ACKNOWLEDGEMENTS

This paper includes data gathered with the 6.5 metre Magellan Telescopes located at Las Campanas Observatory, Chile. This work benefited from discussions conducted during the 'Non-LTE workshop' supported by the National Science Foundation under Grant No. OISE-1927130 (IReNA), the Kavli Institute for Cosmological Physics, and the University of Chicago Data Science Institute. GL is particularly thankful for discussions with Christian Hayes, Keith Hawkins, Kim Venn, and Vini Placco. GL is also indebted to Ása Skúladóttir for her inspiring talk, as well as afterward conversations, at the 2023 CeNAM Frontiers in Nuclear Astrophysics meeting. GL also thanks Zhen Yuan for providing the original LMS-1 members and Ting Li for pointing out the connection between Wukong/LMS-1 and Indus/Jhelum. GL is also sincerely grateful to Yutaka Hirai and Shinya Wanajo for providing the chemical-evolution models.

We thank the anonymous referee whose comments and suggestions contributed to the quality of this paper. GL acknowledges FAPESP (procs. 2021/10429-0 and 2022/07301-5). APJ acknowledges support by the National Science Foundation under grants AST-2206264 and AST-2307599. AC is supported by a Brinson Prize Fellowship at UChicago/KICP. SR thanks support from FAPESP (procs. 2015/50374-0 and 2020/15245-2), CAPES, and CNPq. YST acknowledges financial support from the Australian Research Council through DECRA Fellowship DE220101520. LB acknowledges CAPES/PROEX (proc. 88887.821814/2023-00).

This work has made use of data from the European Space Agency (ESA) mission *Gaia* (https://www.cosmos.esa.int/gaia), processed by the *Gaia* Data Processing and Analysis Consortium (DPAC, https://www.cosmos.esa.int/web/gaia/dpac/consortium). Funding for the DPAC has been provided by national institutions, in particular the institutions participating in the *Gaia* Multilateral Agreement. This research has made use of NASA's Astrophysics Data System Bibliographic Services.

Funding for the Sloan Digital Sky Survey IV has been provided by the Alfred P. Sloan Foundation, the U.S. Department of Energy Office of Science, and the Participating Institutions. SDSS-IV acknowledges support and resources from the Center for High Performance Computing at the University of Utah. The SDSS website is www.sdss.org. SDSS-IV is managed by the Astrophysical Research Consortium for the Participating Institutions of the SDSS Collaboration.

This paper includes data gathered with the 6.5 metre Magellan Telescopes located at Las Campanas Observatory, Chile.

DATA AVAILABILITY

The individual line measurements as well as full abundance tables are provided as supplementary material. All the data, including reduced spectra, plus full line measurements and abundance tables are available at zenodo.org/records/10932808. The code to generate complete abundance tables from SMHR/LESSPAYNE outputs, as well as the redetermined abundances for Indus and Jhelum, can be found at github.com/guilimberg/abund-tables.

REFERENCES

Abbott B. P. et al., 2017a, Phys. Rev. Lett., 119, 161101
Abbott B. P. et al., 2017b, ApJ, 848, L12
Abbott B. P. et al., 2017c, ApJ, 848, L13
Abdurro'uf et al., 2022, ApJS, 259, 35
Aguado D. S. et al., 2021a, MNRAS, 500, 889
Aguado D. S. et al., 2021b, ApJ, 908, L8
Amarante J. A. S., Debattista V. P., Beraldo E Silva L., Laporte C. F. P., Deg N., 2022, ApJ, 937, 12
Aoki W., Beers T. C., Christlieb N., Norris J. E., Ryan S. G., Tsangarides S., 2007, ApJ, 655, 492
Arentsen A., Starkenburg E., Shetrone M. D., Venn K. A., Depagne É., McConnachie A. W., 2019, A&A, 621, A108
Arentsen A., Placco V. M., Lee Y. S., Aguado D. S., Martin N. F., Starkenburg E., Yoon J., 2022, MNRAS, 515, 4082
Asplund M., 2005, ARA&A, 43, 481
Asplund M., Grevesse N., Sauval A. J., Scott P., 2009, ARA&A, 47, 481
Balbinot E., Cabrera-Ziri I., Lardo C., 2022, MNRAS, 515, 5802
Barklem P. S. et al., 2005, A&A, 439, 129
Bastian N., Lardo C., 2018, ARA&A, 56, 83
Beers T. C., Christlieb N., 2005, ARA&A, 43, 531
Beers T. C., Preston G. W., Shectman S. A., 1992, AJ, 103, 1987
Belokurov V. et al., 2006, ApJ, 642, L137
Belokurov V. et al., 2007, ApJ, 658, 337
Belokurov V., Erkal D., Evans N. W., Koposov S. E., Deason A. J., 2018, MNRAS, 478, 611
Bernstein R., Shectman S. A., Gunnels S. M., Mochnacki S., Athey A. E., 2003, in Iye M., Moorwood A. F. M., eds, Proc. SPIE Conf. Ser. Vol. 4841, Instrument Design and Performance for Optical/Infrared Ground-based Telescopes. SPIE, Bellingham, p. 1694
Bisterzo S., Travaglio C., Gallino R., Wiescher M., Käppeler F., 2014, ApJ, 787, 10
Bland-Hawthorn J., Gerhard O., 2016, ARA&A, 54, 529
Bonaca A., Conroy C., Price-Whelan A. M., Hogg D. W., 2019, ApJ, 881, L37
Bonaca A. et al., 2021, ApJ, 909, L26
Bonifacio P. et al., 2020, A&A, 633, A129
Boylan-Kolchin M., Weisz D. R., Johnson B. D., Bullock J. S., Conroy C., Fitts A., 2015, MNRAS, 453, 1503
Boylan-Kolchin M., Weisz D. R., Bullock J. S., Cooper M. C., 2016, MNRAS, 462, L51
Buder S. et al., 2022, MNRAS, 510, 2407
Bullock J. S., Johnston K. V., 2005, ApJ, 635, 931
Burkert A., Forbes D. A., 2020, AJ, 159, 56
Callingham T. M., Cautun M., Deason A. J., Frenk C. S., Grand R. J. J., Marinacci F., 2022, MNRAS, 513, 4107
Cargile P. A., Conroy C., Johnson B. D., Ting Y.-S., Bonaca A., Dotter A., Speagle J. S., 2020, ApJ, 900, 28
Casey A. R., 2014, PhD thesis, Australian National University, Canberra
Casey A. R., Keller S. C., Da Costa G., Frebel A., Maunder E., 2014, ApJ, 784, 19
Castelli F., Kurucz R. L., 2003, in Piskunov N., Weiss W. W., Gray D. F., eds, Proc. IAU Symp. 210, Modelling of Stellar Atmospheres. Cambridge Univ. Press, Cambridge, p. A20
Chiti A., Frebel A., 2019, ApJ, 875, 112
Chiti A., Frebel A., Ji A. P., Jerjen H., Kim D., Norris J. E., 2018, ApJ, 857, 74
Chiti A., Hansen K. Y., Frebel A., 2020, ApJ, 901, 164
Cohen J. G., Huang W., 2009, ApJ, 701, 1053
Cohen J. G., Huang W., 2010, ApJ, 719, 931
Cohen J. G., Christlieb N., Thompson I., McWilliam A., Shectman S., Reimers D., Wisotzki L., Kirby E., 2013, ApJ, 778, 56
Conroy C. et al., 2019, ApJ, 883, 107
Cooper A. P. et al., 2010, MNRAS, 406, 744
Cooper A. P., D'Souza R., Kauffmann G., Wang J., Boylan-Kolchin M., Guo Q., Frenk C. S., White S. D. M., 2013, MNRAS, 434, 3348
Côté B. et al., 2019, ApJ, 875, 106
Cowan J. J., Sneden C., Lawler J. E., Aprahamian A., Wiescher M., Langanke K., Martínez-Pinedo G., Thielemann F.-K., 2021, Rev. Mod. Phys., 93, 015002

Dalessandro E., Lapenna E., Mucciarelli A., Origlia L., Ferraro F. R., Lanzoni B., 2016, ApJ, 829, 77
Dodd E., Callingham T. M., Helmi A., Matsuno T., Ruiz-Lara T., Balbinot E., Lövdal S., 2023, A&A, 670, L2
Drout M. R. et al., 2017, Science, 358, 1570
Eadie G. M., Harris W. E., Springford A., 2022, ApJ, 926, 162
Ezzeddine R. et al., 2020, ApJ, 898, 150
Faber S. M., Gallagher J. S., 1979, ARA&A, 17, 135
Forbes D. A., 2020, MNRAS, 493, 847
Frebel A., 2018, Annu. Rev. Nucl. Part. Sci., 68, 237
Frebel A., Norris J. E., 2015, ARA&A, 53, 631
Frebel A., Casey A. R., Jacobson H. R., Yu Q., 2013, ApJ, 769, 57
Fulbright J. P., 2000, AJ, 120, 1841
Gaia Collaboration 2016a, A&A, 595, A1
Gaia Collaboration 2016b, A&A, 595, A2
Gaia Collaboration 2018, A&A, 616, A1
Gaia Collaboration 2021, A&A, 649, A1
Gaia Collaboration 2023, A&A, 674, A1
Geisler D., Smith V. V., Wallerstein G., Gonzalez G., Charbonnel C., 2005, AJ, 129, 1428
Gratton R., Sneden C., Carretta E., 2004, ARA&A, 42, 385
Hansen T. T., Andersen J., Nordström B., Beers T. C., Placco V. M., Yoon J., Buchhave L. A., 2016, A&A, 586, A160
Hansen T. T. et al., 2021, ApJ, 915, 103
Hasselquist S. et al., 2019, ApJ, 872, 58
Hasselquist S. et al., 2021, ApJ, 923, 172
Hawkins K. et al., 2023, ApJ, 948, 123
Hayes C. R. et al., 2020, ApJ, 889, 63
Haynes C. J., Kobayashi C., 2019, MNRAS, 483, 5123
Haywood M., Di Matteo P., Lehnert M. D., Snaith O., Khoperskov S., Gómez A., 2018, ApJ, 863, 113
Helmi A., White S. D. M., de Zeeuw P. T., Zhao H., 1999, Nature, 402, 53
Helmi A., Babusiaux C., Koppelman H. H., Massari D., Veljanoski J., Brown A. G. A., 2018, Nature, 563, 85
Hill V. et al., 2019, A&A, 626, A15
Horta D. et al., 2023, MNRAS, 520, 5671
Ibata R. A., Gilmore G., Irwin M. J., 1994, Nature, 370, 194
Jablonka P. et al., 2015, A&A, 583, A67
Jacobson H. R. et al., 2015, ApJ, 807, 171
Ji A. P., Frebel A., Chiti A., Simon J. D., 2016a, Nature, 531, 610
Ji A. P., Frebel A., Simon J. D., Chiti A., 2016b, ApJ, 830, 93
Ji A. P. et al., 2020a, AJ, 160, 181
Ji A. P. et al., 2020b, ApJ, 889, 27
Ji A. P. et al., 2023a, AJ, 165, 100
Ji A. P., Naidu R. P., Brauer K., Ting Y.-S., Simon J. D., 2023b, MNRAS, 519, 4467
Johnson B. D. et al., 2020, ApJ, 900, 103
Johnson J. W. et al., 2023, MNRAS, 526, 5084
Johnston K. V., 1998, ApJ, 495, 297
Kauffmann G., White S. D. M., Guiderdoni B., 1993, MNRAS, 264, 201
Kelson D. D., 2003, PASP, 115, 688
Kilpatrick C. D. et al., 2017, Science, 358, 1583
Kirby E. N., Guhathakurta P., Bolte M., Sneden C., Geha M. C., 2009, ApJ, 705, 328
Kirby E. N., Cohen J. G., Smith G. H., Majewski S. R., Sohn S. T., Guhathakurta P., 2011, ApJ, 727, 79
Kobayashi C., Karakas A. I., Lugaro M., 2020, ApJ, 900, 179
Koppelman H. H., Helmi A., Massari D., Roelenga S., Bastian U., 2019a, A&A, 625, A5
Koppelman H. H., Helmi A., Massari D., Price-Whelan A. M., Starkenburg T. K., 2019b, A&A, 631, L9
Koppelman H. H., Bos R. O. Y., Helmi A., 2020, A&A, 642, L18
Kruijssen J. M. D., Pfeffer J. L., Reina-Campos M., Crain R. A., Bastian N., 2019, MNRAS, 486, 3180
Kruijssen J. M. D. et al., 2020, MNRAS, 498, 2472
Larsen S. S., Brodie J. P., Grundahl F., Strader J., 2014, ApJ, 797, 15
Lee Y. S. et al., 2013, AJ, 146, 132
Letarte B. et al., 2010, A&A, 523, A17
Li H. et al., 2022, ApJ, 931, 147
Limberg G. et al., 2021, ApJ, 913, L28
Limberg G., Souza S. O., Pérez-Villegas A., Rossi S., Perottoni H. D., Santucci R. M., 2022, ApJ, 935, 109
Limberg G. et al., 2023, ApJ, 946, 66
Lind K., Asplund M., Barklem P. S., Belyaev A. K., 2011, A&A, 528, A103
Lucatello S., Tsangarides S., Beers T. C., Carretta E., Gratton R. G., Ryan S. G., 2005, ApJ, 625, 825
Lucatello S., Beers T. C., Christlieb N., Barklem P. S., Rossi S., Marsteller B., Sivarani T., Lee Y. S., 2006, ApJ, 652, L37
Lucey M. et al., 2023, MNRAS, 523, 4049
Majewski S. R., Skrutskie M. F., Weinberg M. D., Ostheimer J. C., 2003, ApJ, 599, 1082
Majewski S. R. et al., 2017, AJ, 154, 94
Malhan K., Yuan Z., Ibata R. A., Arentsen A., Bellazzini M., Martin N. F., 2021, ApJ, 920, 51
Malhan K. et al., 2022, ApJ, 926, 107
Maoz D., Mannucci F., 2012, Publ. Astron. Soc. Austr., 29, 447
Marino A. F., Villanova S., Piotto G., Milone A. P., Momany Y., Bedin L. R., Medling A. M., 2008, A&A, 490, 625
Martin N. F. et al., 2022, Nature, 601, 45
Mateu C., 2023, MNRAS, 520, 5225
Matsuno T., Aoki W., Suda T., 2019, ApJ, 874, L35
Matsuno T., Hirai Y., Tarumi Y., Hotokezaka K., Tanaka M., Helmi A., 2021, A&A, 650, A110
Matsuno T., Koppelman H. H., Helmi A., Aoki W., Ishigaki M. N., Suda T., Yuan Z., Hattori K., 2022a, A&A, 661, A103
Matsuno T. et al., 2022b, A&A, 665, A46
Matteucci F., 2012, Chemical Evolution of Galaxies. Springer, Berlin
Matteucci F., Brocato E., 1990, ApJ, 365, 539
Matteucci F., Greggio L., 1986, A&A, 154, 279
McConnachie A. W., 2012, AJ, 144, 4
McMillan P. J., 2017, MNRAS, 465, 76
McWilliam A., Wallerstein G., Mottini M., 2013, ApJ, 778, 149
Milone A. P., Marino A. F., 2022, Universe, 8, 359
Milone A. P. et al., 2017, MNRAS, 464, 3636
Monty S., Venn K. A., Lane J. M. M., Lokhorst D., Yong D., 2020, MNRAS, 497, 1236
Morinaga Y., Ishiyama T., Kirihara T., Kinjo K., 2019, MNRAS, 487, 2718
Mucciarelli A., Origlia L., Ferraro F. R., Pancino E., 2009, ApJ, 695, L134
Myeong G. C., Evans N. W., Belokurov V., Amorisco N. C., Koposov S. E., 2018, MNRAS, 475, 1537
Myeong G. C., Vasiliev E., Iorio G., Evans N. W., Belokurov V., 2019, MNRAS, 488, 1235
Naidu R. P., Conroy C., Bonaca A., Johnson B. D., Ting Y.-S., Caldwell N., Zaritsky D., Cargile P. A., 2020, ApJ, 901, 48
Naidu R. P. et al., 2021, ApJ, 923, 92
Naidu R. P. et al., 2022, preprint (arXiv:2204.09057)
Nidever D. L. et al., 2020, ApJ, 895, 88
Nissen P. E., Schuster W. J., 2010, A&A, 511, L10
Nissen P. E., Schuster W. J., 2011, A&A, 530, A15
Nomoto K., Kobayashi C., Tominaga N., 2013, ARA&A, 51, 457
Norris J. E., Ryan S. G., Beers T. C., 1997, ApJ, 488, 350
Peñarrubia J., Petersen M. S., 2021, MNRAS, 508, L26
Pillepich A., Madau P., Mayer L., 2015, ApJ, 799, 184
Piotto G. et al., 2015, AJ, 149, 91
Placco V. M., Frebel A., Beers T. C., Stancliffe R. J., 2014, ApJ, 797, 21
Placco V. M. et al., 2018, AJ, 155, 256
Placco V. M., Sneden C., Roederer I. U., Lawler J. E., Den Hartog E. A., Hejazi N., Maas Z., Bernath P., 2021, Res. Notes Am. Astron. Soc., 5, 92
Planck Collaboration VI 2020, A&A, 641, A6
Queiroz A. B. A. et al., 2020, A&A, 638, A76
Queiroz A. B. A. et al., 2023, A&A, 673, A155
Reichert M., Hansen C. J., Hanke M., Skúladóttir Á., Arcones A., Grebel E. K., 2020, A&A, 641, A127
de los Reyes M. A. C., Kirby E. N., Ji A. P., Nuñez E. H., 2022, ApJ, 925, 66

Rodríguez-Puebla A., Primack J. R., Avila-Reese V., Faber S. M., 2017, MNRAS, 470, 651
Roederer I. U., Sneden C., Thompson I. B., Preston G. W., Shectman S. A., 2010, ApJ, 711, 573
Roederer I. U., Preston G. W., Thompson I. B., Shectman S. A., Sneden C., Burley G. S., Kelson D. D., 2014, AJ, 147, 136
Rossi S., Beers T. C., Sneden C., 1999, in Gibson B. K., Axelrod R. S., Putman M. E., eds, ASP Conf. Ser. Vol. 165, The Third Stromlo Symposium: The Galactic Halo. Astron. Soc. Pac., San Francisco, p. 264
Rossi S., Beers T. C., Sneden C., Sevastyanenko T., Rhee J., Marsteller B., 2005, AJ, 130, 2804
Schönrich R., Binney J., Dehnen W., 2010, MNRAS, 403, 1829
Searle L., Zinn R., 1978, ApJ, 225, 357
Shappee B. J. et al., 2017, Science, 358, 1574
Sharpe K., Naidu R. P., Conroy C., 2024, ApJ, 963, 11
Shetrone M. D., Côté P., Sargent W. L. W., 2001, ApJ, 548, 592
Shetrone M., Venn K. A., Tolstoy E., Primas F., Hill V., Kaufer A., 2003, AJ, 125, 684
Shipp N. et al., 2018, ApJ, 862, 114
Simon J. D., 2019, ARA&A, 57, 375
Simon J. D., Jacobson H. R., Frebel A., Thompson I. B., Adams J. J., Shectman S. A., 2015, ApJ, 802, 93
Skúladóttir Á., Salvadori S., 2020, A&A, 634, L2
Skúladóttir Á., Tolstoy E., Salvadori S., Hill V., Pettini M., Shetrone M. D., Starkenburg E., 2015, A&A, 574, A129
Skúladóttir Á., Hansen C. J., Salvadori S., Choplin A., 2019, A&A, 631, A171
Skúladóttir Á. et al., 2021, ApJ, 915, L30
Skúladóttir Á., Vanni I., Salvadori S., Lucchesi R., 2024, A&A, 681, A44
Sneden C. A., 1973, PhD thesis, University of Texas, Austin, 0028
Sneden C., Cowan J. J., Gallino R., 2008, ARA&A, 46, 241
Sobeck J. S. et al., 2011, AJ, 141, 175
Springel V., Frenk C. S., White S. D. M., 2006, Nature, 440, 1137
Suda T. et al., 2008, PASJ, 60, 1159
Suda T. et al., 2017, PASJ, 69, 76
Tenachi W., Oria P.-A., Ibata R., Famaey B., Yuan Z., Arentsen A., Martin N., Viswanathan A., 2022, ApJ, 935, L22
Ting Y.-S., Conroy C., Rix H.-W., Cargile P., 2019, ApJ, 879, 69
Tinsley B. M., 1979, ApJ, 229, 1046
Tolstoy E., Hill V., Tosi M., 2009, ARA&A, 47, 371
Travaglio C., Gallino R., Arnone E., Cowan J., Jordan F., Sneden C., 2004, ApJ, 601, 864
Tsujimoto T., 2021, ApJ, 920, L32
Tsujimoto T., Ishigaki M. N., Shigeyama T., Aoki W., 2015, PASJ, 67, L3
Usman S. A. et al., 2024, MNRAS, 529, 2413
Vasiliev E., 2019, MNRAS, 482, 1525
Vasiliev E., Baumgardt H., 2021, MNRAS, 505, 5978
Wanajo S., Hirai Y., Prantzos N., 2021, MNRAS, 505, 5862
White S. D. M., Frenk C. S., 1991, ApJ, 379, 52
Yong D. et al., 2013, ApJ, 762, 26
Yoon J. et al., 2018, ApJ, 861, 146
Yuan Z., Chang J., Beers T. C., Huang Y., 2020, ApJ, 898, L37

SUPPORTING INFORMATION

Supplementary data are available at *MNRAS* online.

Please note: Oxford University Press is not responsible for the content or functionality of any supporting materials supplied by the authors. Any queries (other than missing material) should be directed to the corresponding author for the article.

This paper has been typeset from a TEX/LATEX file prepared by the author.